Supplementary Information Appendix

Fate of $MgSiO_3$ melts at core-mantle boundary conditions

Sylvain Petitgirard[1*], Wim J. Malfait[2], Ryosuke Sinmyo[1], Ilya Kupenko[1,5], Louis Hennet[3], Dennis Harries[4], Thomas Dane[5], Manfred Burghammer[5,6] and David C. Rubie[1]

[1]Bayerisches Geoinstitut, University of Bayreuth, Bayreuth, 95490, Germany
[2] Building Energy Materials and Components, EMPA, Dübendorf, Switzerland
[3] CEMHTI,CNRS, Université d'Orléans, 1d, avenue de la Recherche Scientifique 45071 Orléans Cedex 2 France
[4] Analytical Mineralogy of Micro- and Nanostructures, Institute of Geoscience, Friedrich Schiller University Jena, Carl-Zeiss-Promenade 10, Jena, 07745, Germany
[5] European Synchrotron Radiation Facility, Grenoble, France
[6]Department of Analytical Chemistry, Ghent University, B-9000 Ghent, Belgium

* Corresponding author: Sylvain.petitgirard@uni-bayreuth.de

Sample synthesis and characterization

Glasses were obtained using an aerodynamic set-up in the CEMHTI Lab in Orleans and well described in Auzende *et al.*[1]. Samples were made from a mixture of oxides powder of SiO_2 and MgO (regent grade 99.99%) and ground in a mortar for thirty minutes to achieve a good homogenisation. One gram of the mixture was placed in a pellet die and compacted by applying a load of six tons. The recovered pellet of 1.5 mm thickness and 13 mm in diameter was broken in several parts. A piece of 25 mg was selected and placed in the levitation nozzle to form the glass sphere. An argon flow maintained the compacted powder in levitation, and a CO_2 laser beam was then progressively ramped up to 15% of its maximum power onto the sample (Fig. S1a). A camera and pyrometer helped to monitor the behaviour of the sample while heating up. To completely melt the sample, we had to overshoot the temperature up to 2173 K. The complete melting of the sample was easily identified both with the pyrometer and the live imaging (Fig. S1b). When the sample was entirely molten, the temperature dropped by 200 K and reached a stable plateau at ~1973 K. In the live image, the melting was identified when the sphere passed from an unstable shaky stage to a nice stable sphere. The temperature plateau was kept for 20 seconds; the laser power was then turned off and the sample quenched to room temperature (Fig. S1b). Thanks to the containerless levitation setup, and the resulting absence of nucleation sites, crystallization was avoided during cooling and the samples were quenched into glasses[1].

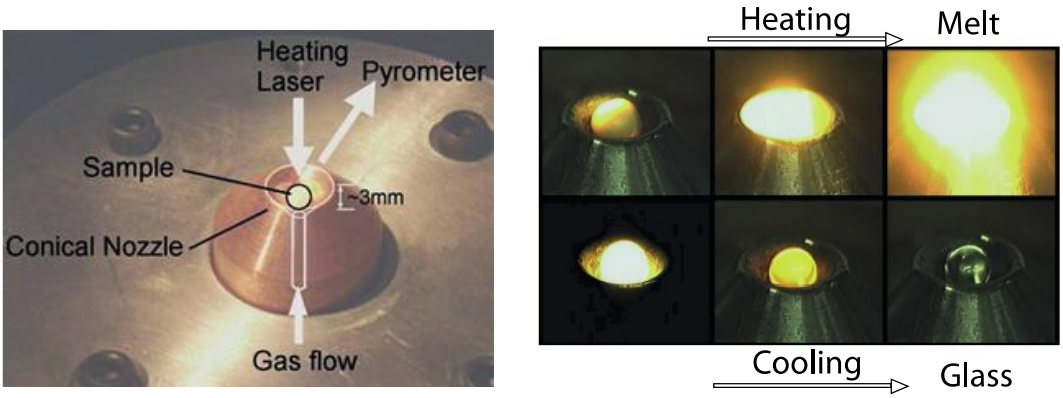

Figure S1. Pictures describing the aerodynamic levitation method to produce homogenous glasses. On the left side, a detailed view and working principal of the aerodynamic levitation chamber is shown. The compressed pellet of oxide powder is levitated with an argon flow while a high-power CO_2 laser melts the entire sample. It is then is rapidly quenched by turning off the power of the laser. Right side, pictures of the melting and quenching process (adapted from Benmore 2012[2]).

One of the spheres was mounted in epoxy and polished for electron microprobe analysis. We carried out a profile analysis and found a constant and homogenous composition for the glass (Table S1). The determined composition ($Mg_{0.98}Si_{1.02}O_3$) is close to the nominal $MgSiO_3$ composition.

SiO2 (mol%)	*MgO (mol%)*	*total*
50.53	49.41	99.94
50.61	49.33	99.94
50.37	49.57	99.94
50.69	49.27	99.95
50.92	49.02	99.94
50.69	49.25	99.94
50.80	49.15	99.95
50.75	49.22	99.96
50.83	49.10	99.93
50.92	49.03	99.95
51.05	48.89	99.94
50.86	49.08	99.95
51.03	48.92	99.94
50.95	49.01	99.96
50.56	49.39	99.95
	Average	
50.77	49.18	99.95

Table S1. Chemical composition of the $MgSiO_3$ sphere along its diameter analysed using a JEOL JXA-8200 electron probe microanalyser installed at BGI and operating at 15 kV, 5 nA and a beam diameter of 30 µm.

Sample preparation and Diamond Anvil Cell loadings

For all the experiments, we used BX-90 type[3] Diamond Anvil Cells (DAC), which allow radial access to the sample. We investigated the full pressure range (0-130 GPa) using two experimental approaches, and prepared two types of Diamond Anvil Cell loadings:

1- For pressures above 30 GPa, we used diamonds of 150 µm culets with 300 µm bevel. After pre-indentation to 20 µm thickness, a hole of 60 µm was drilled in the beryllium gasket and filled with finely ground $MgSiO_3$ glass. The full compaction of the sample is obtained at around 10-15 GPa, and the lowest compression part cannot be investigated with this technique.

2- To circumvent this issue for the lowest pressures from 0 to 25 GPa, we prepared discs of $MgSiO_3$ with sharp vertical edges. A sphere of $MgSiO_3$ was double polished down to 13 µm. After carbon coating the surface, the sample was placed in a FEI Quanta 3D focused ion beam (FIB) workstation and discs were cut from the $MgSiO_3$ plate. We first proceeded by fast milling the discs using a gallium ion beam with a current of 50 nA at 30 keV ion energy. A fine polishing of the side of the discs at 5 nA at 30 keV was then carried out in order to clean the sides and avoid any wedge shape on the side of the disc that could be problematic for finding the edges of the sample during the X-ray absorption experiment (Fig. S2b). We used diamonds of 300 µm culets. The double conical beryllium gasket was pre-indented to 30 µm and a hole of 100 µm was drilled and used as the sample chamber. We placed a $MgSiO_3$ disc recovered from the FIB together with a ~5 µm ruby spheres and we filled the chamber with a methanol:ethanol (4:1) mixture as pressure transmitting medium (Fig. S2c).

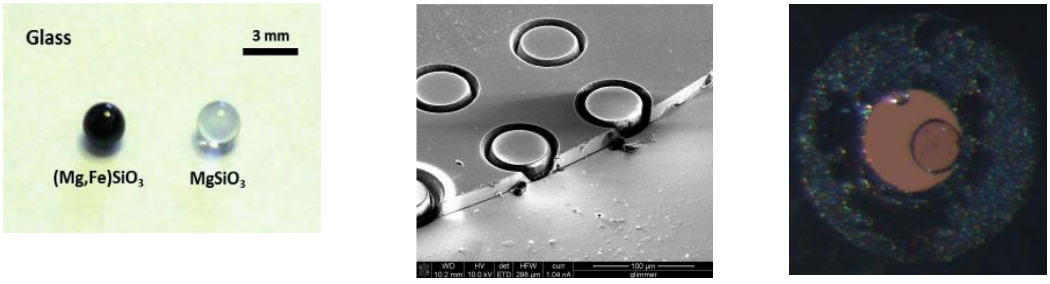

a)-Starting material b)-FIB cutting c)-Loading in ME

Figure S2. Details of the sample preparation for the density measurements in the DAC. a) A pure and homogenous glassy sphere of $MgSiO_3$ is polished down to a thickness of 13 µm and b) discs of 55 µm are cut with an FIB. c) The discs are then loaded in the beryllium gasket with a ruby sphere and methanol-ethanol is employed as pressure-transmitting medium.

X-ray absorption measurements

All measurements were conducted at ID13 beamline (ESRF, France) and we used an X-ray beam set at 13.2 keV focused down to 2x2 µm FWHM using beryllium Compound Reflective Lenses. A description of the beamline components and the geometry of measurements are given in Fig. S3a, S3b. To retrieve the pressure, a portable Raman system was installed at 90 degrees from the incoming X-ray beam (Fig. S3a, S3b).

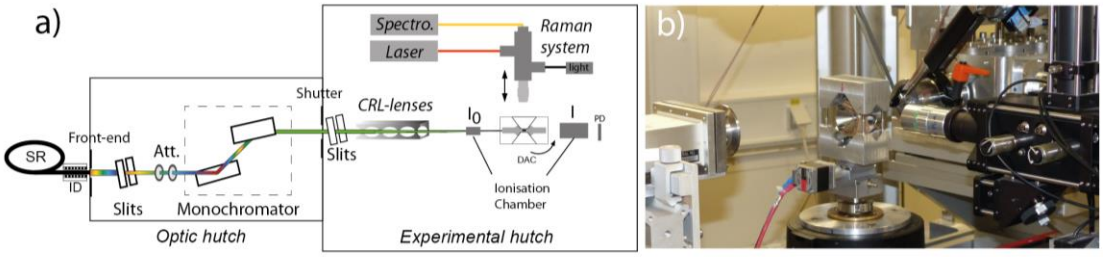

Figure S3. Details of the experimental set-up. a) Schematic drawing of the beamline components and set-up. The undulation of the synchrotron (SR) beam through the insertion device (ID) generates X-rays. In the optic hutch, the X-ray beam is pre-shaped, attenuated and a specific wavelength is selected through a double silicon 111 monochromator. In the experimental hutch, the beam is focus through a set of Be lenses and the absorption is monitored before (I0) and after (I) the sample using ionisation chambers. The pressure is recorded using a portable Raman system set at 90 degrees. b) Picture of the set-up on ID13 with the DAC at the centre, the Raman head on the right side and the ionisation chamber at the back of the DAC.

To measure the density of $MgSiO_3$ at very high pressure, we have adapted the X-ray absorption technique to the confinement of the DAC. The X-ray absorption technique is based on the attenuation of the X-rays through a path length of a material and uses the Beer-Lambert law:

$$-\log_{10}(I/I_0) = (\mu_{HP}.x) \qquad (1)$$

where μ_{HP} is the attenuation coefficient of the sample and contains the absorption linked to its environment (i.e. in our case beryllium) at high pressure, x is the path length, I_0 the intensity of the incoming beam and I the intensity of the beam after the sample. Knowing μ_{HP}, it is then straightforward to calculate the density at high-pressure conditions as the ratios of density over linear absorption coefficient remains the same as that at room conditions with:

$$\rho_{HP} / \mu_{HP} = \rho_0 / \mu_0 \qquad (2)$$

where ρ_{HP} is the density at high pressure, μ_{HP} is calculated from eq.(1), ρ_0 and μ_0 are the density and attenuation coefficient measured at room pressure, respectively. In order to obtain $\mu_{HP,}$ it is necessary to measure precisely the path length of the sample exposed to the X-ray beam, and the intensity of the beam before and after passing through the sample. In large volume presses, the sample is confined in a diamond capsule, and it is assumed that the inner volume stays cylindrical at HP-HT. In the DAC, the sample is not likely to keep its initial shape, and measuring the X-ray attenuation through the diamond is challenging, as the sample is getting very thin. To overcome the two latter points we have used beryllium gaskets to confine the sample to measure its absorbance in the radial geometry and by scanning the sample in the compressional direction we retrieved its dimensions (Main text Fig. 1). The choice of the radial geometry and the use of beryllium is motivated by two points: i) the transmission through 3 mm of beryllium is one order of magnitude higher than through 3 mm of diamond at 13 keV giving a higher absorption contrast and ii) measuring in such geometry enhances the absorbance by using the maximum thickness of sample that can be exposed to the X-rays, i.e. ~50 µm, which is also one order of magnitude higher than in the compression axis (about ~ 5-15 µm). To measure the path length and absorption, our approach was the following:

1- We first map the sample by scanning the DAC with the compressional axis perpendicular to the X-ray beam, in this geometry, we retrieved the X-ray attenuation (I/I_0) through the beryllium gasket (Fig. 1a,b,c main text). This step-by-step mapping is obtained in approximately 30 min.

2- The DAC was then rotated by 90 degrees, and we proceeded to the mapping of the sample through the diamond, with the X-ray parallel to the compression axis. the duration of the mapping is also in the order of 30 min We could then find the path length of sample exposed to the X-rays (Fig.1d,e,f, main text).

3- We combined both sets of maps to correlate the path lengths with their respective absorbance to extract the linear absorbance of the sample at high pressure (Fig.1g main text).

Last but not least, to retrieve the density we also measured the density and absorption at room *P-T* conditions of a standard sample. For this purpose, we measured the attenuation of a double polished $MgSiO_3$ plate with a thickness of 0.697 ± 0.001 mm using the exact same set-up. To avoid any tilting effect of the standard piece of glass, we scanned it at different angles and fit the absorbance as a function of angles (Fig. S4a). The minimum value of the fitted curve is taken as the absorbance of the sample at room conditions (Fig.S4b). The absorbance per mm (μ_0) is then 0.8996 ± 0.0016 mm^{-1}. The density of the double polished glass plate was determined with the sink/float method in a diiodomethane–acetone mixture. The reproducibility for repeated measurements is better than 0.1% and the density of the glass standard was reproduced within 0.5%, and we found a value of 2.770 $g.cm^{-3}$ (ρ_0) for the density at ambient pressure.

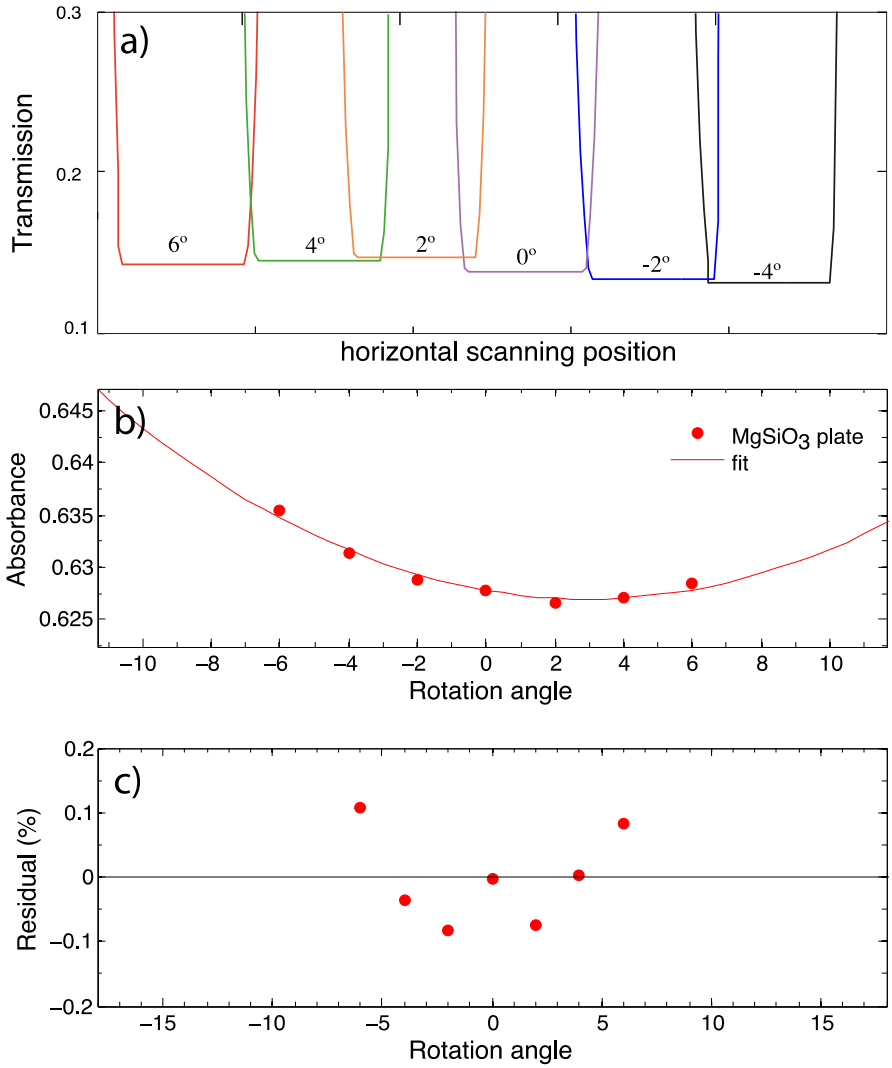

Figure S4. a) X-ray transmission through a 0.697 mm double polished plate of $MgSiO_3$ glass for different angles. b) Fit of the absorbance for the different tilting angles. c) The residual values between data and fit is less than 0.15%.

For pressure determination, we used a portable Raman system set at 90 degrees from the incoming X-ray beam. For the lowest pressure we used the ruby luminescence technique[4], and for the highest pressure, we monitored the Raman signal of diamond from the diamond culet[5]. For pressures between 20 and 60 GPa, we could cross-calibrate both methods, and we obtained similar pressures within less than 1 GPa for the pressure in this regime with both method. We could therefore assume a good confidence for the pressure determination above 60 GPa using the Raman shift as a pressure gauge. As $MgSiO_3$ is a fairly soft and compressible material, as illustrated by the low bulk modulus of 16.9 GPa, the pressure gradient across the sample chamber is fairly small and varies at most of ± 3 GPa for the 2 highest pressure point at 116 ± 3 GPa and 127 ± 3 GPa. It is to be noticed that SiO_2 glass is sometime used as transmitting medium in some other literature examples, although it is not the most hydrostatic one.

Data analysis and Equation of state

All the data were processed through Matlab software. The edges of the sample were determined from the map obtained through the diamond (Fig. SI 5a). This contributes to the

uncertainties on the final densities: as the X-ray beam is not infinitely small, the latter convolute with the edge of the sample. We found an error on the total path length of ± 2 microns, corresponding to ± 1 pixel, for the lowest pressures and up to ± 3 microns at high pressure. However the individual error on each path-length are cancelled out by the high numbers of path-lengths extracted at each pressure points and used to re-calculate the linear absorption fig.S6. The region of interests (ROIs) corresponding to the absorption of the sample as well as the one for the background were set using the absorption map through the beryllium gasket by defining boxes for the background and sample area (Fig. SI 5b). For the highest pressures investigated in this study, cupping of the diamond anvil can occur. On figure 1f (lower panel, main text), we report a profile of the entire diamond culet at 116 GPa and we didn't observe an increase in the absorption at the edge of this profile meaning that if diamond cupping occurs it does not affect the absorption measurements. Indeed, an addition of 10 microns of diamond material in the profile would change the absorption profile of only about 0.15%, because its main constituent, carbon, has a weak absorption at 13 keV.

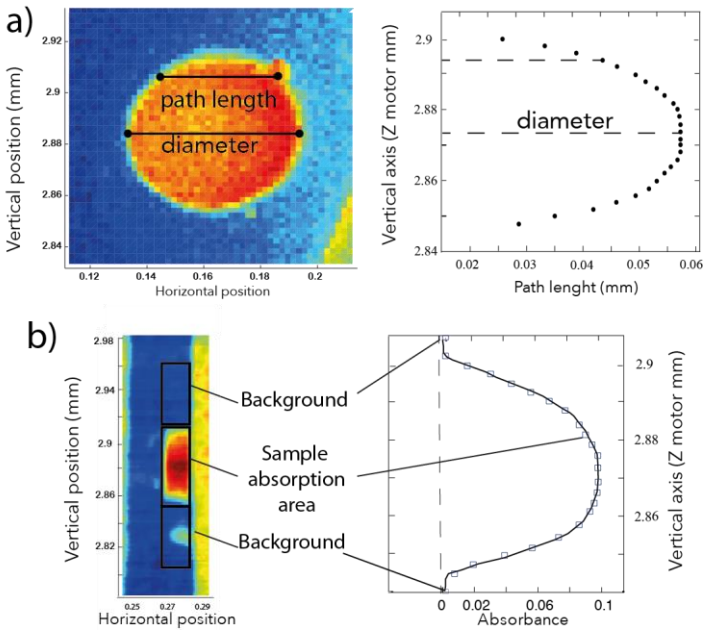

Figure S5. a) Selection of the rim of the sample to retrieve the path length exposed to the X-ray beam. b) Selection of the region of interests (ROIs) for the background and sample absorption, respectively.

Sets of macros repositioned both maps, for vertical coincidence, and calculated the linear absorption (Fig 1g, main text). A correction is added to this latter value and corresponds to the absorbance of the 3 mm of beryllium of the gasket minus the size of the hole (0.1 mm or less depending on the pressure range). We also take into account that a part of the beryllium is not at room conditions and has a higher density, therefore having a higher linear absorption than at room pressure. We assumed that the amount of beryllium that can be considered at high pressure is about 200 µm and 250 µm for the 300 µm and 150/300 µm culets diamond respectively (depending on the size of the sample chamber). We assumed an average pressure for the beryllium between the sample pressure and room pressure, at the side of the culet, and use the equation of state of Lazicki et al[6] to get its density. The linear absorption of the 200-250 µm of beryllium under pressure can be then calculated using the NIST values. In any case, the correction for high-pressure beryllium changes the total value of density of less then 0.5 %.

Loading	P (GPa)	Density (g/cm^3)	molar V (cm^3/mol)
	0.0	2.77 (1)	36.24 (18)
1	29 (1.5)	4.19 (11)	23.9 (6)
1	38 (1.5)	4.29 (11)	23.4 (6)
1	49 (1.5)	4.54 (12)	21.9 (6)
1	57 (1.5)	4.66 (13)	21.3 (6)
2	40 (1.5)	4.32 (12)	22.9 (5)
2	50 (2)	4.74 (13)	21.5 (6)
2	68.5 (2)	4.82 (13)	21.0 (5)
2	79 (2)	4.95 (13)	20.3 (5)
2	89.5 (2)	5.08 (14)	19.7 (5)
2	99 (2)	5.11 (15)	19.3 (6)
2	107 (2.5)	5.29 (16)	18.95 (60)
2	116 (3)	5.32 (21)	18.8 (8)
2	127 (3)	5.37 (21)	18.7 (8)
4	1.0 (5)	2.82 (12)	35.2 (14.3)
4	2.0 (5)	2.91 (12)	34.1 (14.5)
4	4.0 (5)	3.28 (9)	30.6 (9)
4	6 (1)	3.38 (9)	29.7 (8)
4	9.9 (10)	3.56 (10)	28.2 (8)
4	12 (1)	3.66 (10)	27.5 (7.5)
4	25.8 (20)	4.09 (11)	24.3 (6)
4	31 (2)	4.26 (11)	23.54 (6)
6	0.9 (2)	2.96 (8)	35.9 (10)
6	3.1 (5)	3.26 (9)	31.3 (9)
6	5.9 (5)	3.35 (9)	29.9 (8)
6	8.0 (5)	3.53 (9)	28.8 (7)
6	12.6 (5)	3.66 (10)	27.2 (7.5)
6	15.9 (10)	3.78 (10)	26.3 (7)
9	44 (.15)	4.41 (12)	22.7 (6)
9	74 (1.5)	4.82 (13)	20.8 (5)
9	80 (1.5)	4.92 (15)	20.4 (6)

Table S2. Experimental densities, volume and pressures for the different DACs loadings. Values in brackets are the uncertainties on the pressure determination, density and volumes respectively.

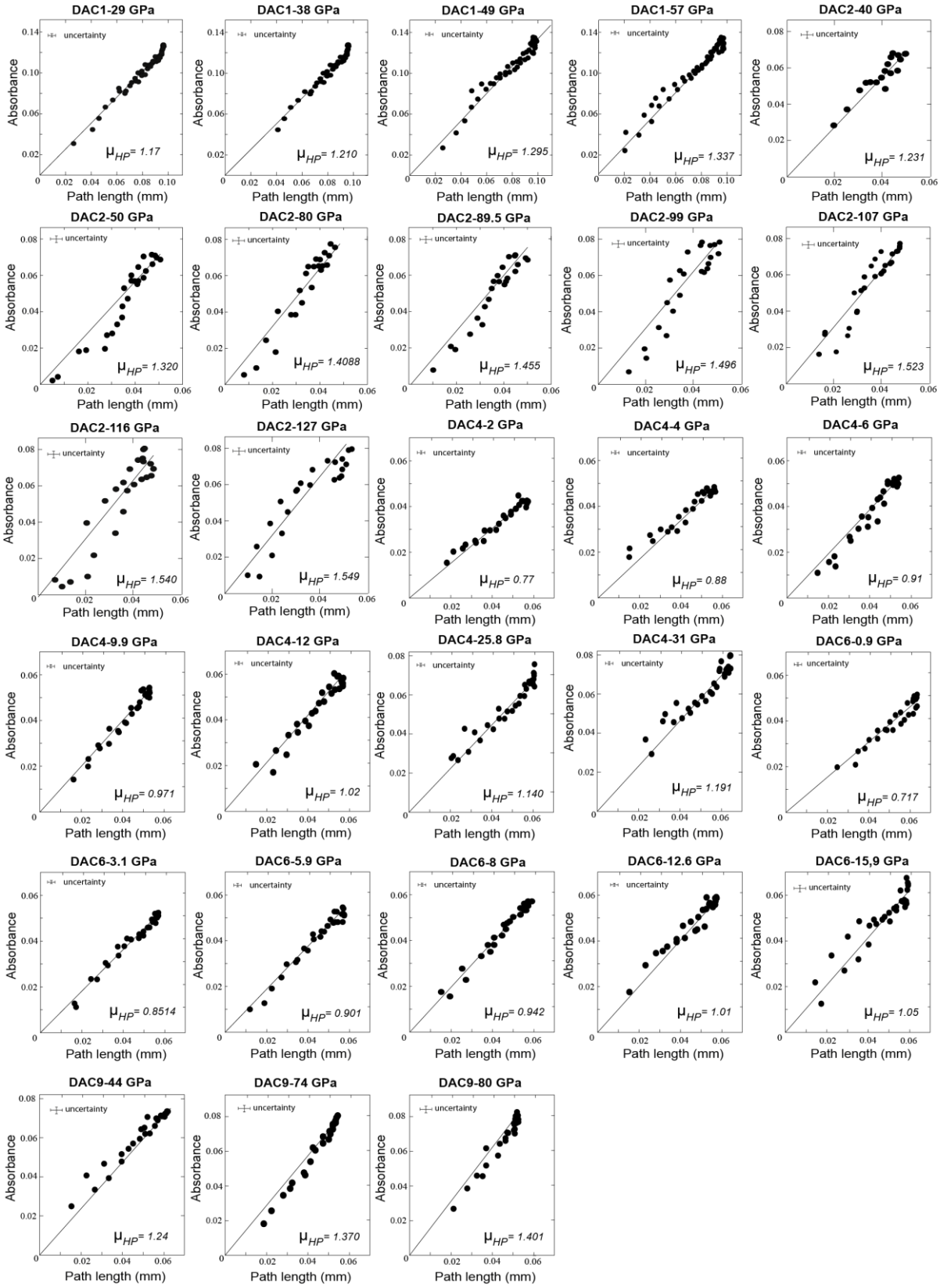

Figure S6. Path-length versus absorbance correlations at high pressure. Values for the absorption are given before the Be correction.

For the equation of state, we converted the density data into molar volume (Table S2). We then fitted the volume as a function of pressure and found the following values for the equation of state: V_0= 36.24 ± 0.36 cm^3/mol, K_{T0}= 16.9 ± 3.2 GPa, K'_{T0} =5.9 ± 1.3, K''_{T0}=-0.004 ± 0.77GPa^{-1}. The correlations between the fit parameters are reported on Fig. S7, with a weak correlation between V_0 and K_{T0} as well between K_{T0} and K'_{T0} but a quite strong one between K'_{T0} and K''_{T0}, giving a higher incertitude for K''_{T0}. We also reported the standard deviation of our data compare to the calculated EoS in fig.2b and we found a deviation of ± 1.2 % indicating that are our data are very well reproduced and described by our EoS. The 95% confidence bands of our EoS are also reported in fig.2b illustrating the very tight confidence intervals for the $MgSiO_3$ EoS. Although some individual points can have larger uncertainty (i.e. at 116 and 127 GPa), the EoS is better constrained because of the large number of points spanning over the entire pressure range, resulting in smaller uncertainties on the EoS than on individual measurements. Last but not least, V_0 is very well constrained by the sink/float measurement and K_{T0} is mostly determined by the points at low pressure from 0 to 40 GPa where the uncertainties are much smaller, providing good constraints on the EoS and improving the extrapolation to higher pressures.

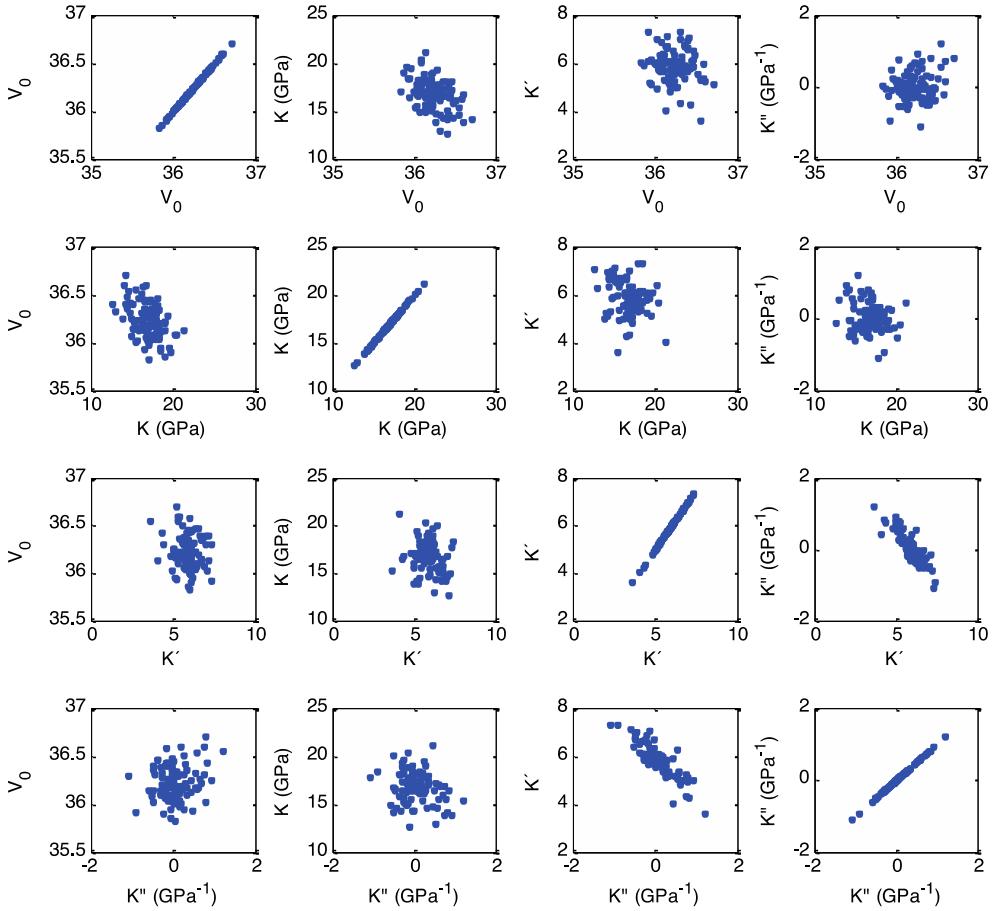

Figure S7. Correlation between parameters of the fourth order Birch-Murnaghan Equation of state used to fit the data.

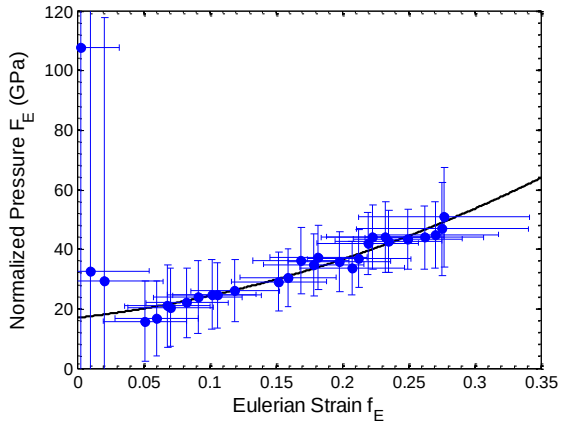

Figure S8. F-f plot of the compression data. Markers denote the experimental data, black line denotes the 4th order BM EoS fitted to the data.

The 4th order Birch-Murnaghan although not completely justify as can be seen from a F-f plot on Fig.S8, we found that it is the best one to represent our dataset over the studied pressure range but also gives values for K_{T0} and K'_{T0} which are the most sensible and closer to the melt at room pressure. We also performed a Vinet fit of our data (Fig.S9) and found values for K_{T0}=14.3± 3.3 GPa and K'_{T0}=8.4± 1.0 with a standard deviation of 1.5%.

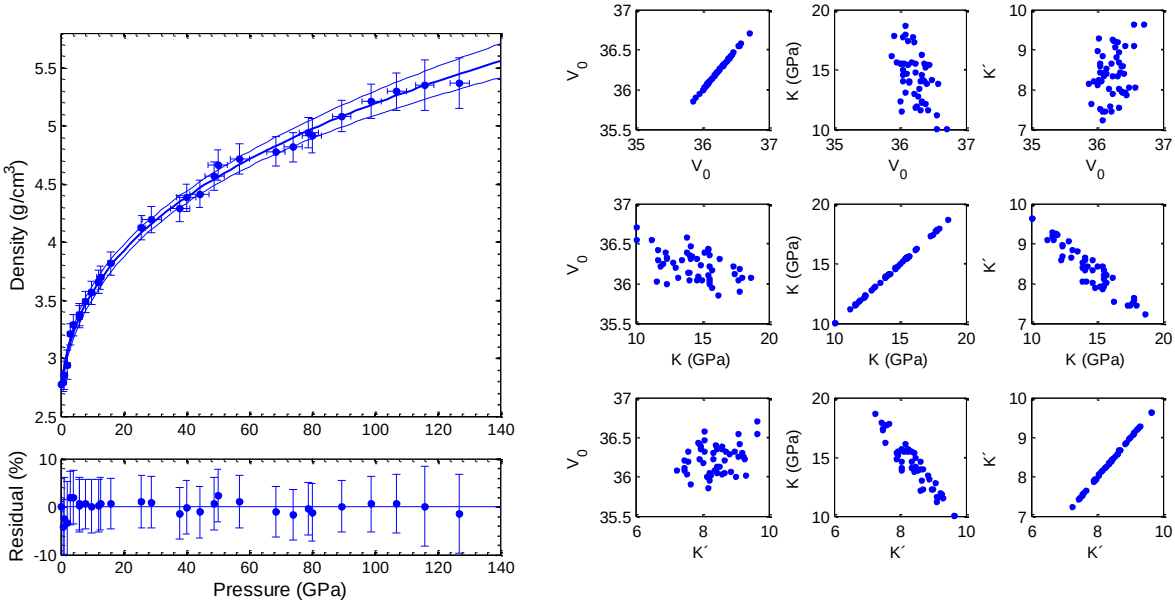

Figure S9. On the left side, Vinet EoS fit through the data (thick line) with 95% confidence interval (thin lines). On the right side, Correlation between the Vinet EoS fit parameters.

Calculation of melts densities

From the fourth order BM equation-of-state, we could re-calculate the density of amorphous $MgSiO_3$ at high temperature along different isotherms. We used the formula of Stixrude and Karki 2005[7] to extrapolate the density of melts at high temperature with:

$$P(V,T) = P_c(V,T_0) + P_{th}(V,T) = P_c(V,T_0) + \gamma C_V/V\,(T-T_0) \qquad (3)$$

$$\text{and} \quad \gamma C_V/V\,(T-T_0) = \alpha K_T\,(T-T_0) \qquad (4)$$

We found the values for αK_T reported in de Koker and Stixrude 2009[8] the most appropriate as they vary only with pressure but seem independent of the temperature. We could fit the αK_T value using a power law curve (Fig.S8) (i.e. similar to the expression for gamma[9]).

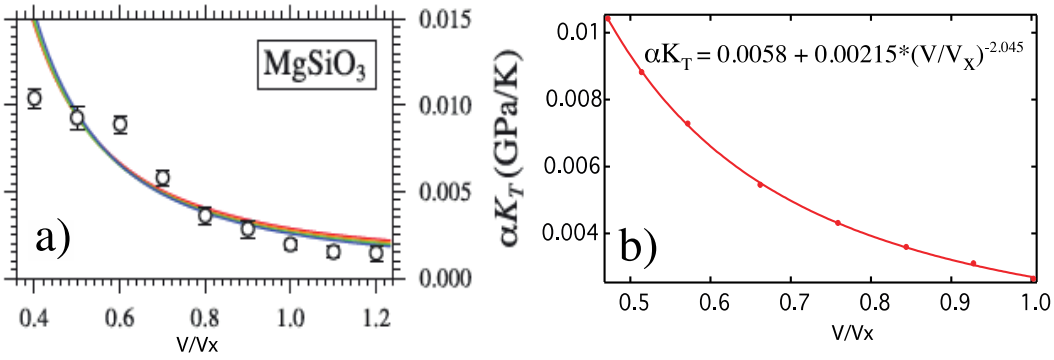

Figure S10. a) plot extracted from de Koker and Stixrude[8] b) fit of the data to obtain the thermal expansion parameter for the high temperature calculations.

As mentioned in the main text and in fig.3a and using parameters from fig.S10, we found a very close agreement with the densities calculated at 3000 K[10] , and at 4000 K[8,9]. Also reported on fig.S11 are the data form shock experiments for similar composition[11–13]. Although difficult to compare, as they do not follow an isothermal path like in the calculations, at high pressure the densities found from shock compression on $MgSiO_3$ melts are very close to the one we found at 4000 K. It has to be noticed, that such an agreement between calculation, shock compression and static compression is rarely obtained in high pressure science and gives good confidence on the very high density of glasses and melts at very high pressure.

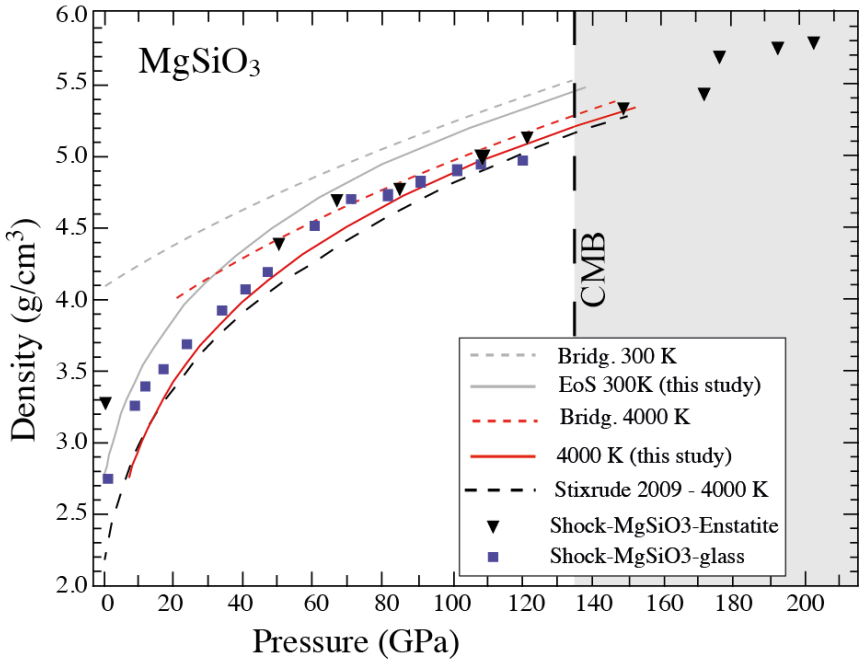

Figure S11. $MgSiO_3$ density data as a function of pressure from different studies. In full and dashed grey lines, densities for $MgSiO_3$ bridgmanite and glass (this study) at 300 K respectively. In full and dashed red lines, $MgSiO_3$ bridgmanite and melt (this study) at 4000 K respectively. The dashed black curve is the density for $MgSiO_3$ melt at 4000 K from Stixrude et al. 2009[9]. The black triangles are the

density data for melts derived form shock experiment from enstatite starting material[12] and purple squares from $MgSiO_3$ glass starting material[13] and where melting was observed.

Calculation of the density crossover.

For the density crossover calculation, we assumed a simple binary system between $MgSiO_3$ and $FeSiO_3$. In this case, the density contrast between the solid and liquid phase is linked to the iron-partitioning coefficient between both phases with:

$$K_D = \{X(FeSiO_3^{Sol})/X(MgSiO_3^{Sol})\}/\{X(FeSiO_3^{Liq})/X(MgSiO_3^{Liq})\} \quad (5)$$

And the resulting densities for both the iron-enriched liquid: $Mg_{1-x}Fe_xSiO_3^{Liq}$ and the depleted solid: $Mg_{1-y}Fe_ySiO_3^{Sol}$ can be expressed as a liner combination for the liquid: (1-x) $MgSiO_3^{Liq}$ + x $FeSiO_3^{Liq}$ and in a same way for the solid with :(1-y) $MgSiO_3^{Sol}$ + y $FeSiO_3^{Sol}$ We assumed a bulk composition of $(Mg_{0.9}Fe_{0.1})SiO_3$ and calculated the amount of iron in each phase, for different iron portioning coefficient ranging from 0.1 to 0.5. The composition for each phase in eq(5) for various partitioning coefficient are reported in table S4.

K_D	Mg# (solid)	Mg# (liquid)	Mg# (bulk)
0.1	97.9	82.1	90
0.2	96.3	83.7	90
0.3	95.0	85.0	90
0.4	93.9	86.1	90
0.5	93.0	87.0	90

Table S4. Calculation of the iron content in the solid and liquid phases for different partitioning coefficient K_D. The calculation gives the proportion for each end-members for both the solid and liquid phases in eq(5) expressed as Mg number (Mg#).

We used our density model at 4000 K to get the density of the liquid $MgSiO_3$. For the density of the $FeSiO_3$ liquid, we used the data computed by Ramo *et al.*[14] and for the solid end-members, $MgSiO_3$ and $FeSiO_3$ respectively; we used the equation of state at 4000 K using the parameters reported by Xu *et al*[15]. The results of the density for each phases, solid and liquid, and density contrast between resulting solid and liquid for variable partitioning of iron are given in Table S5 and plotted in Fig.3b (main text).

P (GPa)	Density of Liquid-Phase (g/cm^3)					Density of Solid-Phase (g/cm^3)					Density difference (g/cm^3)				
	K0.1	K0.2	K0.3	K0.4	K0.5	K0.1	K0.2	K0.3	K0.4	K0.5	Δρ K0.1	Δρ K0.2	Δρ K0.3	Δρ K0.4	Δρ K0.5
25	3.694	3.677	3.665	3.654	3.645	4.067	4.085	4.1	4.112	4.122	-0.373	-0.408	-0.435	-0.458	-0.477
35	3.962	3.945	3.932	3.921	3.911	4.232	4.251	4.266	4.279	4.289	-0.27	-0.306	-0.334	-0.358	-0.378
45	4.274	4.258	4.246	4.235	4.226	4.38	4.399	4.414	4.427	4.438	-0.105	-0.141	-0.169	-0.192	-0.211
55	4.458	4.441	4.428	4.417	4.408	4.46	4.47	4.487	4.501	4.512	-0.002	-0.029	-0.059	-0.084	-0.104
65	4.622	4.605	4.591	4.579	4.57	4.637	4.657	4.673	4.686	4.698	-0.015	-0.053	-0.083	-0.107	-0.128
75	4.766	4.748	4.734	4.722	4.712	4.752	4.773	4.789	4.802	4.814	0.014	-0.025	-0.055	-0.081	-0.102
85	4.909	4.891	4.876	4.863	4.853	4.86	4.881	4.898	4.911	4.923	0.049	0.01	-0.022	-0.048	-0.07
95	5.029	5.009	4.994	4.981	4.97	4.962	4.983	5.001	5.014	5.025	0.066	0.026	-0.006	-0.033	-0.056
105	5.146	5.126	5.11	5.097	5.085	5.059	5.08	5.097	5.111	5.123	0.087	0.045	0.012	-0.015	-0.038
115	5.256	5.236	5.219	5.205	5.194	5.151	5.173	5.19	5.204	5.216	0.105	0.063	0.029	0.001	-0.022
125	5.353	5.332	5.315	5.301	5.289	5.24	5.261	5.279	5.293	5.305	0.113	0.07	0.036	0.008	-0.016
135	5.444	5.422	5.405	5.391	5.388	5.324	5.346	5.364	5.378	5.391	0.12	0.076	0.041	0.012	-0.002
145					5.477					5.472					0.005
155					5.558					5.55					0.008

Table S5. Density contrast between solid and liquid $MgFeSiO_3$ for various iron partitioning coefficient (K). The density for the liquid phase and solid phase are calculated with different amount of iron as describe in table S4. The difference in density in the last 5 columns marks the pressure where density crossover between an iron rich liquid and an iron-depleted solid as a result of partial melting is expected.

References:

1. Auzende, A.-L. *et al.* Synthesis of amorphous MgO-rich peridotitic starting material for laser-heated diamond anvil cell experiments - application to iron partitioning in the mantle. *High Press. Res.* **31,** 199–213 (2011).
2. Benmore, C. A Review of High-Energy X-Ray Diffraction from Glasses and Liquids. *ISRN Mat. Sci.* (2012).
3. Kantor, I. *et al.* BX90: A new diamond anvil cell design for X-ray diffraction and optical measurements. *Rev. Sci. Instrum.* **83,** (2012).
4. Mao, H. K., Xu, J. & Bell, P. M. Calibration of the ruby pressure gauge to 800-kbar under quasi-hydrostatic conditions. *J. Geophys. Res.* **91,** 4673–4676 (1986).
5. Akahama, Y. & Kawamura, H. Pressure calibration of diamond anvil Raman gauge to 310 GPa. *J. Appl. Phys.* **100,** (2006).
6. Lazicki, A., Dewaele, A., Loubeyre, P. & Mezouar, M. High-pressure-temperature phase diagram and the equation of state of beryllium. *Phys. Rev. B* **86,** (2012).
7. Stixrude, L. & Karki, B. Structure and freezing of MgSiO3 liquid in Earth's lower mantle. *Science (80-.).* **310,** 297–299 (2005).
8. De Koker, N. & Stixrude, L. Self-consistent thermodynamic description of silicate liquids, with application to shock melting of MgO periclase and $MgSiO_3$ perovskite. *Geophys. J. Int.* **178,** 162–179 (2009).
9. Stixrude, L., de Koker, N., Sun, N., Mookherjee, M. & Karki, B. Thermodynamics of silicate liquids in the deep Earth. *Earth Planet. Sci. Lett.* **278,** 226–232 (2009).
10. Ghosh, D. B., Karki, B. & Stixrude, L. First-principles molecular dynamics simulations of $MgSiO_3$ glass: Structure, density, and elasticity at high pressure. *Am. Miner.* **99,** 1304–1314 (2014).
11. Mosenfelder, J. L., Asimow, P. D., Frost, D. J., Rubie, D. C. & Ahrens, T. J. The MgSiO3 system at high pressure: Thermodynamic properties of perovskite, postperovskite, and melt from global inversion of shock and static compression data. *J. Geophys. Res.* **114,** (2009).
12. Akins, J. A., Luo, S.-N., Asimow, P. D. & Ahrens, T. J. Shock induced melting of MgSiO3 perovskite and implications for melts in Earth's lowermost mantle. *Geophys. Res. Lett.* L14612 (2003).
13. Luo, S.-N., Akins, J. A., Ahrens, T. J. & Asimow, P. D. Shock compressed $MgSiO_3$ glass, enstatite, olivine, and quartz: Optical emission, temperatures, and melting. *J. Geophys. Res.* **109,** B05205 (2004).
14. Ramo, D. M. & Stixrude, L. Spin crossover in Fe_2SiO_4 liquid at high pressure. *Geophys. Res. Lett.* **41,** 4512–4518 (2014).
15. Xu, W., Lithgow-Bertelloni, C., Stixrude, L. & Ritsema, J. The effect of bulk composition and temperature on mantle seismic structure. *Earth Planet. Sci. Lett.* **275,** 70–79 (2008).